https://doi.org/10.26599/FRICT.2026.9441282

Research Article

A spherical-coordinate grease lubrication model for wear evolution of miter gate bottom pivot bearings

Shuai Cheng [a, b], Qihang Wang [c], Zhe Wang [a, b], Zehua Han [a, b], Zhaonan Liu [a, b], Xianghui Meng [a, b, *]

a. State Key Laboratory of Mechanical System and Vibration, Shanghai Jiao Tong University, Shanghai 200240, China

b. School of Mechanical Engineering, Shanghai Jiao Tong University, Shanghai 200240, China

c. Changjiang Survey, Planning, Design, and Research Co., Ltd., Wuhan 430010, China

Xianghui Meng, Email: xhmeng@sjtu.edu.cn

Received: October 1, 2025; Revised: June 19, 2026; Accepted: July 6, 2026

Abstract

The bottom pivot (spherical bearing and pintle) of miter gates operates under low-speed, ultra-heavy load conditions, where wear is unavoidable. Recent hydraulic projects have adopted grease injection to improve lubrication, yet the absence of models tailored to spherical friction pairs limits understanding of its mechanism and effectiveness. To address this, a non-Newtonian grease lubrication model in spherical coordinates, coupled with bearing elastic deformation, is developed to simulate mixed elastohydrodynamic conditions. Wear evolution is investigated with dry friction as a reference. Long-term tests on a scaled pivot rig demonstrate that grease lubrication reduces the maximum wear depth by approximately 39.5% after 16000 cycles and provides substantial protection to the lateral surface. Close agreement between simulated and experimental results for both wear distribution and depth validates the proposed model. It is important to note that grease lubrication can inhibit the formation of solid lubricant transfer films. Therefore, periodic maintenance is essential during long-term operation to prevent friction pair performance deterioration once the grease degrades and the protective transfer film becomes insufficient.

Keywords

Bottom pivot bearing; Grease lubrication; Spherical coordinate; Wear evolution.

1. Introduction

The miter gate in a hydro-junction navigation lock is a key component for regulating upstream and downstream water levels and ensuring safe vessel passage. As shown in Fig. 1, the spherical bearing and spherical pintle at the bottom pivot serve as the main load-bearing and rotating elements of the gate [1-3]. Due to the large mass of the miter gate leaf and the turbid, sediment-laden river water, the bottom pivot bearing operates long-term under ultra-heavy loads and low rotational speeds, along with harsh conditions such as high humidity and particle erosion [4, 5]. These factors make it prone to wear failures, which severely compromise operational safety and structural stability [6, 7].

In engineering practice, solid self-lubricating materials are commonly embedded in the bearing surface to provide basic lubrication and ensure smooth operation of the bottom pivot [8-10]. To further reduce friction and wear, grease is periodically applied to form a fluid film and improve lubrication. However, due to the pivot's unique structure and harsh operating environment, the effectiveness of grease remains uncertain, making it difficult to evaluate its advantages over dry friction. Therefore, theoretical and experimental studies are needed to clarify the influence of grease on bearing wear behavior.

Previous theoretical studies have examined the factors influencing the tribological performance of miter gate bottom pivot bearings, including the properties of solid lubricants [11], mechanical characteristics of the substrate [12], and friction and wear behavior [13]. These studies suggest that under dry or solid lubrication conditions, the formation of transfer films, bearing stress-strain responses, and operating conditions all have significant effects on bearing wear. However, modeling and mechanistic studies on pivot bearings under grease lubrication remain limited. In lubrication modeling of spherical friction pairs, artificial hip joints are a typical subject of study. Scholars have developed simulation models based on the Reynolds equation in spherical coordinates to investigate wear behavior [14] and surface texture effects [15] in artificial hip joints. Xu et al. [16] also applied a similar lubrication modeling approach for grease lubrication in spherical bearings. However, these studies use Reynolds equations based on Newtonian fluids and fail to account for the non-Newtonian characteristics of grease. It is also important to note that most non-Newtonian grease lubrication models are developed in Cartesian or cylindrical coordinate systems. For example, Li et al. [17] employed a Reynolds equation based on the Ostwald model to investigate the effects of operating parameters and surface roughness on temperature rise and tribological behavior of grease-lubricated bearings under heavy loads. Wang et al. [18] studied the lubrication and wear of roller tooth surfaces in harmonic drives using a line-contact grease Reynolds equation and a wear model. Cheng et al. [19] developed a rotor dynamics framework and a grease elastohydrodynamic lubrication (EHL) model to analyze the influence of bushing elastic modulus on rotor system performance. Nevertheless, lubrication models for grease in spherical coordinates remain underexplored, which presents challenges for modeling bottom pivot bearings.

Experimental research has systematically assessed the friction, wear, and vibration behavior of miter gate friction pairs for fault diagnosis. For example, Zhao et al. [20] developed a multi-notch chord length method for indirectly measuring wear on hemispherical friction surfaces and validated it using a scaled gate test rig to achieve rapid evaluation of spherical bearing wear. Mei et al. [21] collected vibration signals of the top pivot reinforcement plate before and after the overhaul of the Gezhou Dam ship lock, and applied various signal processing and analysis techniques to study fault diagnosis methods. Qin et al. [22] used a friction tester to investigate the tribological behavior of miter gate bottom pivot pairs under grease lubrication at varying contact stresses, finding that ploughing dominated when the actual stress was below the allowable limit, while adhesive wear prevailed otherwise. These platforms replicate the loading, rotational speed, and lubrication conditions of bottom pivots, making them well-suited for evaluating tribological performance and validating simulation models.

Under heavy loads, bottom pivot bearings experience significant elastic deformation, which directly affects lubrication and contact states. Accurate modeling thus requires incorporating structural elastic feedback. The deformation influence coefficient matrix method is widely regarded as a reliable approach [23, 24]. It involves precomputing the compliance matrix via finite element software, integrating it into lubrication and contact calculations to obtain instantaneous deformation, which is then fed back into the film thickness. This process iterates until convergence of pressure and elastic deformation is achieved. This method has been widely applied and validated in the deformation analysis of sliding bearings and their components [25-27], yet existing simulations of bottom pivots still lack detailed consideration of transient elastic deformation.

In summary, current lubrication theories for bottom pivot bearings lack a non-Newtonian grease model in spherical coordinates and a clear understanding of wear evolution under grease-lubricated conditions. This study aims to derive a Reynolds equation for grease in spherical coordinates and incorporate transient bearing deformation to establish a mixed elasto-hydrodynamic lubrication model. Based on this model, the influence of grease on the wear behavior of bottom pivot bearings will be evaluated, with dry friction conditions serving as a reference. Long-term wear tests on scaled bearing specimens will be carried out using a custom-designed test rig. The findings will provide theoretical support for the design and service life prediction of miter gate bottom pivots.

Fig. 1 Schematic diagram of the bottom pivot friction pair of miter gates.

2. Theoretical model

This section introduces the derivation of the grease lubrication model in spherical coordinates, as well as the modeling of rough surface contact, elastic deformation, wear evolution, and the numerical calculation methods.

2.1. Grease lubrication modeling in spherical coordinates

As a typical non-Newtonian fluid, grease is often characterized by rheological models that capture its nonlinear behavior. The Herschel-Bulkley (HB) model is widely considered accurate for this purpose, and is expressed as [28, 29]:

$$\tau = \tau_s + \eta^* \cdot \dot{\gamma}^n \qquad (1)$$

where τ, τ_s, $\dot{\gamma}$, η^*, and n represent the shear stress, yield stress, shear rate, plastic viscosity, and rheological index, respectively. When the local τ is below τ_s, the grease forms a stationary solidified layer. A flowing layer develops only when τ exceeds τ_s, allowing shear flow. Given that the influence of τ_s becomes negligible under high-shear conditions [30, 31], its effect is often omitted in practical lubrication analysis. Therefore, the simplified Ostwald model ($\tau_s = 0$) is typically employed [32, 33], which is expressed as:

$$\tau = \eta^* \cdot \dot{\gamma}^n \qquad (2)$$

The grease is characterized using a DHR-20 rheometer (TA Instruments, USA) through shear tests to obtain the shear stress-shear rate relationship. A cone-plate geometry with a 40 mm diameter and a cone angle of 1.0 ° is employed (Fig. 2a), with a test gap of 25 μm. Measurements are conducted at 40 °C, corresponding to the average temperature during long-term tests, over a shear rate range of 0.1~15000 s^{-1}. The results indicate that the grease exhibits pronounced nonlinear behavior, as shown in Fig. 2 (b). Fitting the data with the HB model yields $\eta^* = 0.112\ (\mathrm{Pa} \cdot \mathrm{s})^n$ and $n = 0.804$.

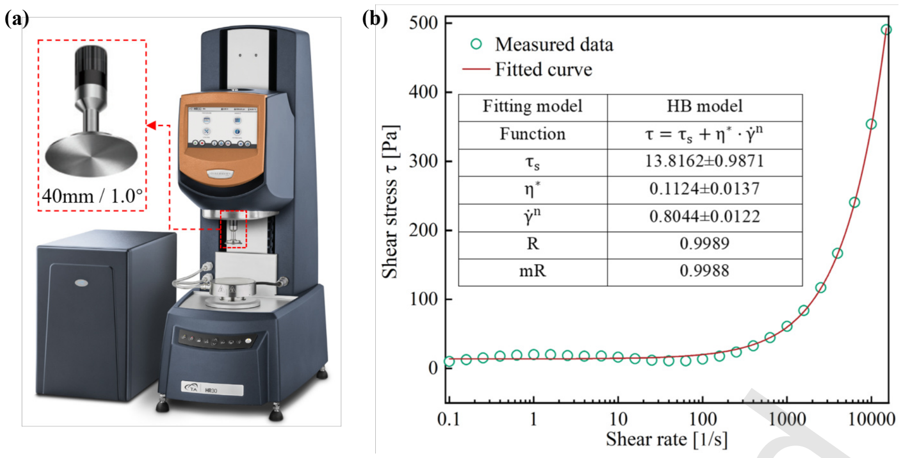

Fig. 2 Rheological behavior of the lubricating grease: (a) testing instrument; (b) measured and fitted data.

The spherical coordinate system is defined as shown in Fig. 3, where the sphere has a radius R, the latitude direction is θ with the z-axis at $\theta = 0$, and the longitude direction is φ with the x-axis at $\varphi = 0$. The displacement of the sphere within the spherical shell is defined as $\mathbf{e} = [e_x, e_y, e_z]^T$.

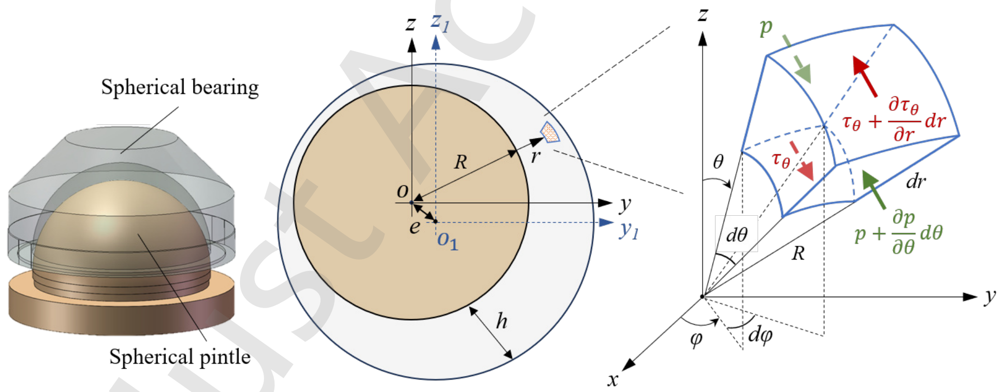

Fig. 3 Force diagram of a fluid element in spherical coordinates.

Consider a fluid element located on the spherical surface. In the θ direction, the cross-section of the element can be approximated as a rectangle with side lengths of $R\sin\theta\, d\varphi$ and dr, where dr is a small increment in the film thickness direction. Thus, the cross-sectional area is $A_\theta = R\sin\theta\, d\varphi \cdot dr$. The pressure on one side of the element is p, and on the other side is $p + \frac{\partial p}{\partial \theta} d\theta$. The resulting pressure force difference in the θ direction is:

$$F_p = \left[\left(p + \frac{\partial p}{\partial \theta} d\theta\right) - p\right] \mathrm{A}_\theta = \frac{\partial p}{\partial \theta} \mathrm{d}\theta \cdot \mathrm{R} \sin\theta \, \mathrm{d}\varphi \mathrm{d}r \quad (3)$$

Let τ_θ denote the shear stress in the θ direction. Due to its variation along the r direction, a shear force is generated by the difference in shear stress between the upper and lower surfaces of the fluid element. The shear stress on the inner surface is τ_θ, and on the outer surface is $\tau_\theta + \frac{\partial \tau_\theta}{\partial r} \mathrm{d}r$. The cross-sectional area in the r direction is $\mathrm{A_r} = \mathrm{R}\mathrm{d}\theta \cdot \mathrm{R} \sin\theta \, \mathrm{d}\varphi$. Therefore, the shear force difference in the θ direction is:

$$F_\tau = \left[\left(\tau_\theta + \frac{\partial \tau_\theta}{\partial r} dr\right) - \tau_\theta\right] \mathrm{A_r} = \frac{\partial \tau_\theta}{\partial r} \mathrm{d}r \cdot \mathrm{R}\mathrm{d}\theta \cdot \mathrm{R} \sin\theta \, \mathrm{d}\varphi \quad (4)$$

The force balance in the θ direction yields:

$$\frac{\partial p}{\partial \theta} \mathrm{d}\theta \cdot \mathrm{R} \sin\theta \, \mathrm{d}\varphi \mathrm{d}r = \frac{\partial \tau_\theta}{\partial r} \mathrm{d}r \cdot \mathrm{R}\mathrm{d}\theta \mathrm{R} \sin\theta \, \mathrm{d}\varphi \quad (5)$$

Dividing both sides of the above equation by $\mathrm{R}^2 \sin\theta \, \mathrm{d}\theta \mathrm{d}\varphi \mathrm{d}r$, we obtain the general position-dependent relation:

$$\frac{\partial \tau_\theta}{\partial r} = \frac{1}{\mathrm{R}} \frac{\partial p}{\partial \theta} \quad (6)$$

Similarly, analysis in the φ direction yields:

$$\frac{\partial \tau_\varphi}{\partial r} = \frac{1}{\mathrm{R} \sin\theta} \frac{\partial p}{\partial \varphi} \quad (7)$$

Based on Eq. (6), combining the Ostwald model with the velocity gradient yields:

$$\frac{\partial \tau_\theta}{\partial r} = \frac{\partial}{\partial r}\left[\eta^* \left(\frac{\partial u_\theta}{\partial r}\right)^n\right] = \frac{1}{R} \frac{\partial p}{\partial \theta} \quad (8)$$

Integrating the above equation with respect to r gives:

$$\frac{\partial u_\theta}{\partial r} = \left(\frac{r}{\eta^* R} \frac{\partial p}{\partial \theta}\right)^{\frac{1}{n}} + \mathrm{C}_1 \quad (9)$$

Integrating again yields:

$$u_\theta = \frac{n}{n+1} \left(\frac{1}{\eta^* R} \frac{\partial p}{\partial \theta}\right)^{\frac{1}{n}} r^{\frac{n+1}{n}} + \mathrm{C}_1 r + \mathrm{C}_2 \quad (10)$$

Applying the boundary conditions: when $r = 0$，$u_\theta = U_{\theta 1}$ (velocity of the sphere), when $r = h$, $u_\theta = U_{\theta 2}$ (velocity of the shell), results in:

$$C_1 = \frac{U_{\theta 2}-U_{\theta 1}}{h} - \frac{n}{n+1}\left(\frac{1}{\eta^* R}\frac{\partial p}{\partial \theta}\right)^{\frac{1}{n}} h^{\frac{1}{n}}\ ,\ C_2 = U_{\theta 1} \tag{11}$$

Substituting into the general solution gives:

$$u_\theta = \frac{n}{n+1}\left(r^{\frac{n+1}{n}} - rh^{\frac{1}{n}}\right)\left(\frac{1}{\eta^* R}\frac{\partial p}{\partial \theta}\right)^{\frac{1}{n}} + \frac{U_{\theta 2}-U_{\theta 1}}{h} r + U_{\theta 1} \tag{12}$$

Similarly, based on the constitutive equation and the relationship between shear stress and pressure gradient in the φ direction, the following expression can be obtained:

$$u_\varphi = \frac{n}{n+1}\left(r^{\frac{n+1}{n}} - rh^{\frac{1}{n}}\right)\left(\frac{1}{\eta^* R\sin\theta}\frac{\partial p}{\partial \varphi}\right)^{\frac{1}{n}} + \frac{U_{\varphi 2}-U_{\varphi 1}}{h} r + U_{\varphi 1} \tag{13}$$

The flow rates in the θ and φ directions are defined as q_θ and q_φ, respectively, given by:

$$q_\theta = \int_0^h u_\theta\, dr = \int_0^h \left[\frac{n}{n+1}\left(r^{\frac{n+1}{n}} - rh^{\frac{1}{n}}\right)\left(\frac{1}{\eta^* R}\frac{\partial p}{\partial \theta}\right)^{\frac{1}{n}} + \frac{U_{\theta 2}-U_{\theta 1}}{h} r + U_{\theta 1}\right] \mathrm{d}r$$

$$= \frac{n}{n+1}\left(\frac{1}{\eta^* R}\frac{\partial p}{\partial \theta}\right)^{\frac{1}{n}}\left(\frac{n}{2n+1} h^{\frac{2n+1}{n}} - \frac{1}{2} h^{\frac{2n+1}{n}}\right) + \frac{h}{2}\left(U_{\theta 1} + U_{\theta 2}\right)$$

$$= \frac{n}{n+1}\left(\frac{1}{\eta^* R}\frac{\partial p}{\partial \theta}\right)^{\frac{1}{n}}\left(\frac{-1}{4n+2}\right) h^{\frac{2n+1}{n}} + \frac{h}{2}\left(U_{\theta 1} + U_{\theta 2}\right) \tag{14}$$

$$q_\varphi = \int_0^h u_\varphi\, dr = \frac{n}{n+1}\left(\frac{1}{\eta^* R\sin\theta}\frac{\partial p}{\partial \varphi}\right)^{\frac{1}{n}}\left(\frac{-1}{4n+2}\right) h^{\frac{2n+1}{n}} + \frac{h}{2}\left(U_{\varphi 1} + U_{\varphi 2}\right) \tag{15}$$

According to the law of mass conservation in spherical coordinates, the rate of mass change within a fluid element per unit time is equal to the difference between the inflow and outflow mass fluxes, that is:

$$\frac{1}{\mathrm{R}\sin\theta}\frac{\partial(\sin\theta\rho q_\theta)}{\partial\theta} + \frac{1}{\mathrm{R}\sin\theta}\frac{\partial \rho q_\varphi}{\partial\varphi} + \frac{\partial \rho h}{\partial t} = 0 \tag{16}$$

Substituting the expressions of q_θ and q_φ into the mass conservation equation yields:

$$\frac{1}{R\sin\theta}\frac{\partial}{\partial\theta}\left[\sin\theta\frac{1}{4n+2}\cdot\frac{n}{n+1}h^{\frac{2n+1}{n}}\cdot\left(\frac{1}{\eta^* R}\frac{\partial p}{\partial \theta}\right)^{\frac{1}{n}}\right] + \frac{1}{R\sin\theta}\frac{\partial}{\partial\varphi}\left[\frac{1}{4n+2}\cdot\frac{n}{n+1}h^{\frac{2n+1}{n}}\left(\frac{1}{\eta^* R\sin\theta}\frac{\partial p}{\partial \varphi}\right)^{\frac{1}{n}}\right]$$

$$= \frac{1}{2R\sin\theta}\frac{\partial \sin\theta(U_{\theta 1}+U_{\theta 2})h}{\partial\theta} + \frac{1}{2R\sin\theta}\frac{\partial\left(U_{\varphi 1}+U_{\varphi 2}\right)h}{\partial\varphi} + \frac{\partial h}{\partial t} \tag{17}$$

For the bottom pivot friction pair, the bearing is in motion while the pintle remains stationary. The relative motion can be represented by U_θ and U_φ, leading to the following expressions:

$$\frac{1}{R\sin\theta}\frac{\partial}{\partial\theta}\left[\sin\theta\frac{1}{4n+2}\cdot\frac{n}{n+1}h^{\frac{2n+1}{n}}\cdot\left(\frac{1}{\eta^{*}R}\frac{\partial p}{\partial\theta}\right)^{\frac{1}{n}}\right]+\frac{1}{R\sin\theta}\frac{\partial}{\partial\varphi}\left[\frac{1}{4n+2}\cdot\frac{n}{n+1}h^{\frac{2n+1}{n}}\left(\frac{1}{\eta^{*}R\sin\theta}\frac{\partial p}{\partial\varphi}\right)^{\frac{1}{n}}\right]$$

$$=\frac{1}{2R\sin\theta}\frac{\partial\sin\theta U_\theta h}{\partial\theta}+\frac{1}{2R\sin\theta}\frac{\partial U_\varphi h}{\partial\varphi}+\frac{\partial h}{\partial t} \qquad (18)$$

The motion of the bottom pivot bearing occurs as rotation within the x-y plane, meaning it only has an angular velocity about the z-axis, denoted as ω_z. Therefore:

$$\begin{cases} U_\theta = 0 \\ U_\varphi = R\omega_z\sin\theta \end{cases} \qquad (19)$$

Substituting this into the relevant equations and using ω in place of ω_z, Eq. (19) becomes:

$$\frac{1}{4n+2}\cdot\frac{n}{n+1}\cdot\left(\frac{1}{R}\right)^{\frac{1}{n}}\cdot\frac{\partial}{\partial\theta}\left[\sin\theta\, h^{\frac{2n+1}{n}}\cdot\left(\frac{1}{\eta^{*}}\frac{\partial p}{\partial\theta}\right)^{\frac{1}{n}}\right]+\frac{1}{4n+2}\cdot\frac{n}{n+1}\cdot\left(\frac{1}{R\sin\theta}\right)^{\frac{1}{n}}\cdot\frac{\partial}{\partial\varphi}\left[h^{\frac{2n+1}{n}}\left(\frac{1}{\eta^{*}}\frac{\partial p}{\partial\varphi}\right)^{\frac{1}{n}}\right]$$

$$=\frac{1}{2}R\omega\sin\theta\frac{\partial h}{\partial\varphi}+R\sin\theta\frac{\partial h}{\partial t} \qquad (20)$$

When $n = 1$, the above equation reduces to the Reynolds equation for Newtonian fluids [34, 35], thereby demonstrating the validity of the model, as shown below:

$$\frac{1}{12R}\cdot\frac{\partial}{\partial\theta}\left(\sin\theta\frac{h^3}{\eta^{*}}\frac{\partial p}{\partial\theta}\right)+\frac{1}{12R\sin\theta}\cdot\frac{\partial}{\partial\varphi}\left(\frac{h^3}{\eta^{*}}\frac{\partial p}{\partial\varphi}\right)=\frac{1}{2}R\omega\sin\theta\frac{\partial h}{\partial\varphi}+R\sin\theta\frac{\partial h}{\partial t} \qquad (21)$$

It is worth noting that when considering the effect of surface roughness on fluid lubrication, flow factors are introduced into the Reynolds equation [36, 37]. However, the influence of flow factors on film pressure is significant only when the film thickness is very small, and can be neglected for large-scale, large-clearance friction pairs such as the bottom pivot. Admittedly, flow factors applicable to grease lubrication in spherical coordinates may be investigated in future studies to enable accurate simulation of precision friction pairs.

The film thickness in spherical coordinates h can be expressed as:

$$h = \mathrm{C} - e_x \sin\theta \cos\varphi - e_y \sin\theta \sin\varphi - e_z \cos\theta + d_h + h_{wear} \quad (22)$$

where C denotes the radial clearance; d_h and h_{wear} represent the surface elastic deformation and wear depth, respectively, which will be detailed in the following section. Over the computational domain, the resultant force generated by the fluid pressure is calculated by the following integral:

$$\begin{cases} F_{gx} = R^2 \int_{\varphi_1}^{\varphi_2} \int_{\theta_1}^{\theta_2} p\,(\sin\theta)^2 \cos\varphi \, d\theta d\varphi \\ F_{gy} = R^2 \int_{\varphi_1}^{\varphi_2} \int_{\theta_1}^{\theta_2} p\,(\sin\theta)^2 \sin\varphi \, d\theta d\varphi \\ F_{gz} = R^2 \int_{\varphi_1}^{\varphi_2} \int_{\theta_1}^{\theta_2} p \cos\theta \sin\theta \, d\theta d\varphi \end{cases} \quad (23)$$

2.2. Rough surface contact modeling

The KE model [38, 39] is used to calculate p_c, and the expression is as follows:

$$p_c(h^*) = \frac{2}{3}\mathrm{KH_b}\pi(\xi\beta\sigma)\begin{bmatrix} \delta_c^{*-0.5} \int_{h^*}^{h^*+\delta_c^*} \delta^{*1.5}\,\Psi(z^*)\,dz^* \\ +1.03\delta_c^{*-0.425} \int_{h^*+\delta_c^*}^{h^*+6\delta_c^*} \delta^{*1.425}\,\Psi(z^*)\,dz^* \\ +1.4\delta_c^{*-0.263} \int_{h^*+6\delta_c^*}^{h^*+110\delta_c^*} \delta^{*1.263}\,\Psi(z^*)\,dz^* \\ +\frac{3}{K} \int_{h^*+110\delta_c^*}^{\infty} \delta^{*1}\,\Psi(z^*)\,dz^* \end{bmatrix} \quad (24)$$

where h^*, δ^* and z^* denote the dimensionless film thickness, relative interference between asperities, and equivalent height of asperities, respectively. The parameters ξ and β represent the equivalent density and curvature radius of the surface asperities. $\mathrm{H_b}$ refers to the Brinell hardness of the softer material, while the hardness coefficient $\mathrm{K} = 0.454 + 0.41\nu$, where ν is the Poisson's ratio of the softer material. $\Psi(\mathrm{z}^*)$ describes a dimensionless probability density function based on a Gaussian distribution, $\Psi(\mathrm{z}^*) = 1/\sqrt{2\pi}\,\mathrm{e}^{-\mathrm{z}^{*2}/2}$. The critical interference δ_c and its dimensionless form $\delta_c{}^*$ are given as:

$$\begin{cases} \delta_c = \left(\frac{\pi K H_b}{2E}\right)^2 \beta \\ \delta_c^* = \left(\frac{\pi K H_b}{2E}\right)^2 \frac{\beta}{\sigma} \end{cases} \tag{25}$$

In this expression, $\mathrm{E} = \frac{1}{\left[\frac{1-\nu_1{}^2}{\mathrm{E}_1}+\frac{1-\nu_2{}^2}{\mathrm{E}_2}\right]}$, where the subscripts 1 and 2 refer to the two contact surfaces. The specific material parameters are listed in Table 1.

2.3. Elastic deformation modeling

Elastic deformation is calculated based on the principle of linear superposition, which requires extracting the compliance matrix of the bottom pivot bearing. As shown in Fig. 4, a scaled-down model of the bottom pivot bearing (1:10) is imported into the finite element software. After a mesh independence test, the model is discretized with 24400 hexahedral elements (on the sides) and 800 wedge elements (on the top). Fixed constraints are applied to the outer surface of the bearing, and a uniform pressure is applied to the inner surface in a static analysis. This ensures the bearing remains in the elastic deformation range, and the deformation influence coefficients obtained are used to construct the compliance matrix.

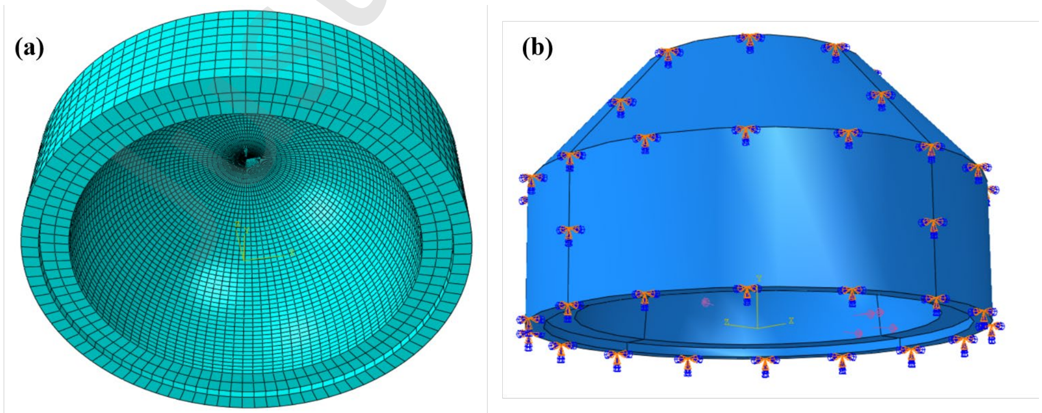

Fig. 4 Compliance matrix extraction of the bottom pivot bearing specimen: (a) mesh generation; (b) application of constraints.

The elastic deformation d_h of nodes can be calculated using the principle of linear superposition:

$$d_h(i,j) = \sum_{\mathrm{e=1}}^{\mathrm{e=m}} \sum_{\mathrm{f=1}}^{\mathrm{f=n}} \mathrm{D}_{\mathrm{i,j}}^{\mathrm{e,f}} [p(\mathrm{e,f}) + p_c(\mathrm{e,f})]\, \mathrm{dA} \tag{26}$$

where $\mathrm{D}_{\mathrm{i,j}}^{\mathrm{e,f}}$ represents the influence coefficient of the force at node $(\mathrm{e,f})$ on the deformation at node $(\mathrm{i,j})$, dA denotes the corresponding mesh area, and the detailed expression of the compliance matrix $\boldsymbol{D}$, which accounts for deformations in the x, y, and z directions at all nodes, is given below.

$$\boldsymbol{D} = \begin{bmatrix} {D_{xx}}_{1,1}^{1,1} & {D_{yx}}_{1,1}^{1,1} & {D_{zx}}_{1,1}^{1,1} & {D_{xx}}_{1,1}^{2,1} & {D_{yx}}_{1,1}^{2,1} & {D_{zx}}_{1,1}^{2,1} & \cdots & {D_{xx}}_{1,1}^{m,n} & {D_{yx}}_{1,1}^{m,n} & {D_{zx}}_{1,1}^{m,n} \\ {D_{xy}}_{1,1}^{1,1} & {D_{yy}}_{1,1}^{1,1} & {D_{zy}}_{1,1}^{1,1} & {D_{xy}}_{1,1}^{2,1} & {D_{yy}}_{1,1}^{2,1} & {D_{zy}}_{1,1}^{2,1} & \cdots & {D_{xy}}_{1,1}^{m,n} & {D_{yy}}_{1,1}^{m,n} & {D_{zy}}_{1,1}^{m,n} \\ {D_{xz}}_{1,1}^{1,1} & {D_{yz}}_{2,1}^{1,1} & {D_{zz}}_{1,1}^{1,1} & {D_{xz}}_{1,1}^{2,1} & {D_{yz}}_{1,1}^{2,1} & {D_{zz}}_{1,1}^{2,1} & \cdots & {D_{xz}}_{1,1}^{m,n} & {D_{yz}}_{1,1}^{m,n} & {D_{zz}}_{1,1}^{m,n} \\ {D_{xx}}_{2,1}^{1,1} & {D_{yx}}_{2,1}^{1,1} & {D_{zx}}_{2,1}^{1,1} & {D_{xx}}_{2,1}^{2,1} & {D_{yx}}_{2,1}^{2,1} & {D_{zx}}_{2,1}^{2,1} & \cdots & {D_{xx}}_{2,1}^{m,n} & {D_{yx}}_{2,1}^{m,n} & {D_{zx}}_{2,1}^{m,n} \\ {D_{xy}}_{2,1}^{1,1} & {D_{yy}}_{2,1}^{1,1} & {D_{zy}}_{2,1}^{1,1} & {D_{xy}}_{2,1}^{2,1} & {D_{yy}}_{2,1}^{2,1} & {D_{zy}}_{2,1}^{2,1} & \cdots & {D_{xy}}_{2,1}^{m,n} & {D_{yy}}_{2,1}^{m,n} & {D_{zy}}_{2,1}^{m,n} \\ {D_{xz}}_{2,1}^{1,1} & {D_{yz}}_{2,1}^{1,1} & {D_{zz}}_{2,1}^{1,1} & {D_{xz}}_{2,1}^{2,1} & {D_{yz}}_{2,1}^{2,1} & {D_{zz}}_{2,1}^{2,1} & \cdots & {D_{xz}}_{2,1}^{m,n} & {D_{yz}}_{2,1}^{m,n} & {D_{zz}}_{2,1}^{m,n} \\ \vdots & \vdots & \vdots & \vdots & \vdots & \vdots & \ddots & \vdots & \vdots & \vdots \\ {D_{xz}}_{m,n}^{1,1} & {D_{yz}}_{m,n}^{1,1} & {D_{zz}}_{m,n}^{1,1} & {D_{xy}}_{m,n}^{2,1} & {D_{yz}}_{m,n}^{2,1} & {D_{zz}}_{m,n}^{2,1} & \cdots & {D_{xz}}_{m,n}^{m,n} & {D_{yz}}_{m,n}^{m,n} & {D_{zz}}_{m,n}^{m,n} \end{bmatrix} \tag{27}$$

2.4. Wear evolution modeling

According to Archard wear model [40], the wear depth h_{wear} of the bearing can be expressed as [41, 42]:

$$h_{wear} = \frac{\mathrm{C_w}}{\mathrm{H_b}} \cdot W_L \cdot \mathrm{t_{step}} \tag{28}$$

where $\mathrm{C_w}$ and $\mathrm{H_b}$ are the wear coefficient and hardness of the bearing respectively, and $\mathrm{t_{step}}$ is the relevant step time. The wear load W_L is the average value of the product of contact pressure and sliding velocity in a rotation cycle $\mathrm{T_{cyc}}$:

$$W_L = \frac{1}{\mathrm{T_{cyc}}} \int_{\mathrm{t}}^{\mathrm{t+T_{cyc}}} p_c |\mathrm{U}| \mathrm{dt} \tag{29}$$

Superimposing the distributions of the p_c in one cycle can obtain the wear position within one cycle, and further obtaining the h_{wear} according to Eq. (28).

Determining the $\mathrm{C_w}$ of the friction pair is crucial for the Archard model, and this study uses an experimental calibration method to obtain it. Specifically, pre-tests are conducted on the bottom pivot samples using a dedicated test rig under dry friction and grease lubrication conditions, with 3000 cycles for each. The maximum h_{wear} in the heavily worn regions is measured with a high-precision 3D coordinate measuring machine. Simultaneously, W_L is calculated using the Archard model. The $\mathrm{C_w}$ values for both conditions are then calibrated based on the experimental h_{wear} and the accumulated W_L from 3000 simulation cycles. The resulting $\mathrm{C_w}$ values are 2.54×10^{-6} for dry friction and 2.50×10^{-6} for grease lubrication.

Incorporating h_{wear} into the bearing clearance accounts for wear evolution's impact on the tribological performance of the bearing. However, updating the clearance every cycle has a minimal effect and reduces computational efficiency. To address this, a wear acceleration strategy is adopted. After calculating h_{wear} per cycle and assuming that the contact state remains unchanged within the acceleration interval, h_{wear} per cycle is accumulated linearly to obtain the cumulative wear corresponding to the number of acceleration cycles. This cumulative value is then added to the bearing clearance, and the subsequent calculation is performed based on the updated geometry. The simulation results (Fig. 5) show that h_{wear} of the bottom pivot bearing after one cycle is 2.79 nm. When the acceleration factor is set to 200, 500, and 1000, the maximum h_{wear} after 1001 cycles is 2.71 μm, 2.76 μm, and 2.79 μm, respectively. It can be observed that the error between the results obtained with acceleration factors of 1000 and 200 is within 3%, which is acceptable, and the wear distributions from both cases are nearly identical, indicating that updating wear depth using an acceleration factor of 1000 does not compromise the accuracy of the wear evolution. Therefore, in the present model, t_{step} is set as the time required for the bearing to complete 1000 cycles. The material and surface parameters of the bottom pivot friction pair are listed in Table 1.

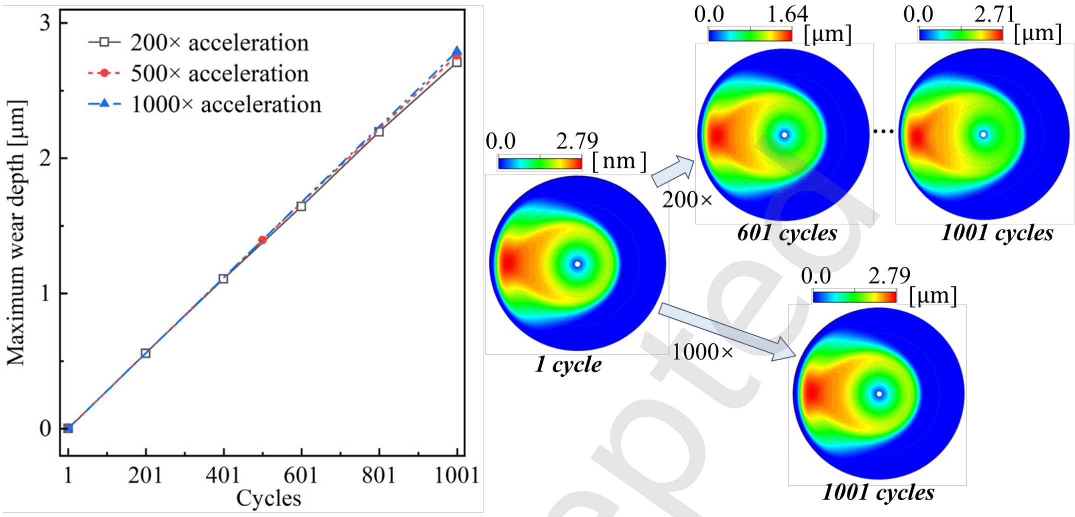

Fig. 5 Maximum wear depth of bottom pivot bearing under different acceleration factors.

Table 1. Material and surface parameters of bottom pivot bearing.

Parameters	Values
Elastic modulus of bearing and pintle (E_1, E_2)	105GPa, 546GPa
Poisson ratio of bearing and pintle (ν_1, ν_2)	0.35, 0.3
Density of bearing and pintle (ρ_1, ρ_2)	7800 kg/m^3, 7850 kg/m^3
Equivalent deviation of roughness (σ)	1.414 μm
Asperity density (ξ)	0.009 μm^{-2}

Equivalent curvature of asperity (β)	3.733 μm
Wear coefficient (C_w)	2.54×10^{-6}
Wear coefficient with grease (C_w)	2.50×10^{-6}
Hardness (H_b)	2.2 GPa

2.5. Numerical solution method

To solve the equilibrium displacement of a nonlinear mechanical system under static loading in three-dimensional space, a Newton–Raphson iterative framework is established. The equilibrium condition of the system can be expressed as:

$$\mathbf{R}(\mathbf{e}) = \mathbf{F}(\mathbf{e}) - \mathbf{W} \tag{30}$$

where $\mathbf{R} = [R_x, R_y, R_z]^T$ is the residual force vector, $\mathbf{F} = [F_x, F_y, F_z]^T$ represents the combined hydrodynamic and contact forces, $\mathbf{W} = [W_x, W_y, W_z]^T$ denotes the external load.

The Newton–Raphson method is employed to update the displacement vector as follows:

$$\mathbf{e}^{k+1} = \mathbf{e}^{k} - \mathbf{J}^{-1}(\mathbf{e}^{k})\mathbf{R}(\mathbf{e}^{k}) \tag{31}$$

where k denotes the iteration step number, $\mathbf{J}$ is the Jacobian matrix, representing the sensitivity of the force vector to the displacement at the current iteration [43].

$$\mathbf{J} = \begin{bmatrix} \frac{\partial F_x}{\partial e_x} & \frac{\partial F_x}{\partial e_y} & \frac{\partial F_x}{\partial e_z} \\ \frac{\partial F_y}{\partial e_x} & \frac{\partial F_y}{\partial e_y} & \frac{\partial F_y}{\partial e_z} \\ \frac{\partial F_z}{\partial e_x} & \frac{\partial F_z}{\partial e_y} & \frac{\partial F_z}{\partial e_z} \end{bmatrix} \tag{32}$$

A relative tolerance $\varepsilon_R = 10^{-4}$ is defined, and the convergence criterion for the iteration is:

$$\frac{||\mathbf{R}^{k}||}{||\mathbf{W}||} < \varepsilon_R \tag{33}$$

The proposed framework is based on dynamic analysis and incorporates a mixed EHL model, explicitly accounting for the non-Newtonian behavior of grease in a spherical coordinate system. It enables the coupled simulation of lubrication, contact, deformation, and wear evolution in the bottom pivot friction pair, thereby improving the prediction of long-term wear evolution. The numerical framework is implemented independently using Fortran, with the computational workflow illustrated in Fig. 6.

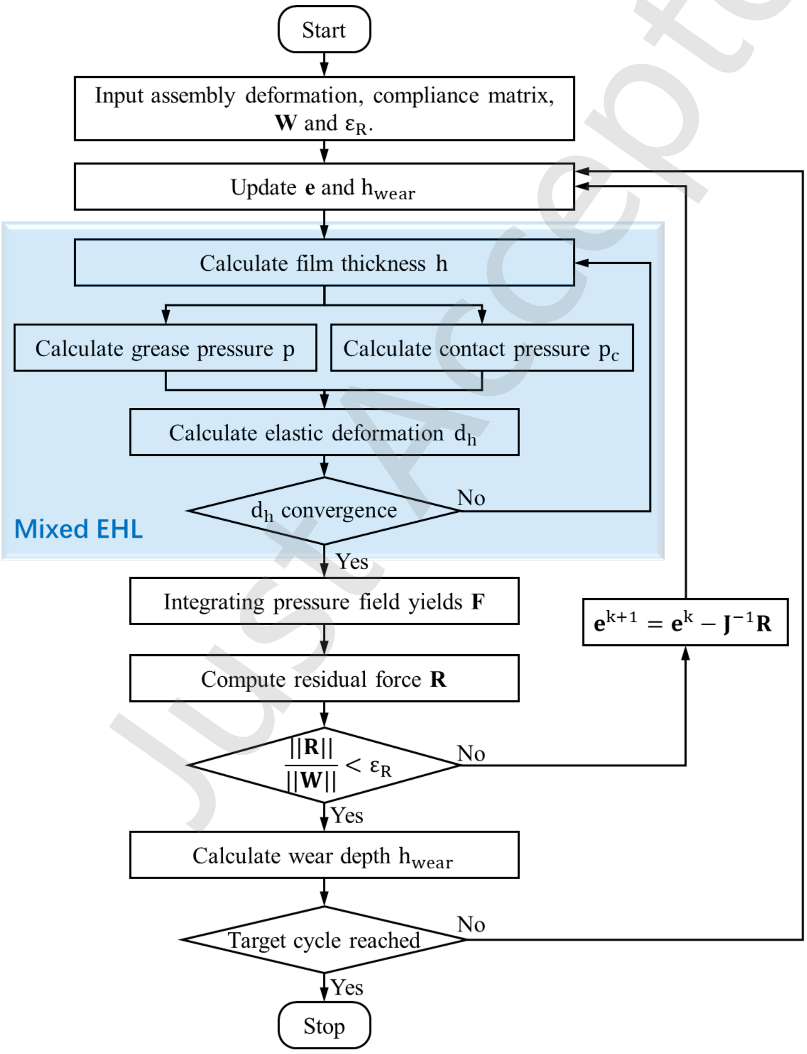

Fig. 6 Flowchart of the numerical procedure.

Step 1: Input the deformation matrix, assemble deformation, external loads **W**, convergence tolerance ε_R, and structural/material parameters.

Step 2: Update the displacement vector $\mathbf{e}$ and wear depth h_{wear}, and calculate the film thickness h accordingly.

Step 3: Solve for the grease film pressure p and contact pressure p_c based on the current h.

Step 4: Calculate the elastic deformation d_h caused by pressure and iterate until the pressure and deformation converge.

Step 5: Integrate the p and p_c to obtain forces $\mathbf{F}$. Construct the residual vector $\mathbf{R}$ based on the difference between the $\mathbf{F}$ and $\mathbf{W}$.

Step 6: Determine whether the residual satisfies the convergence criterion. If not, apply the Newton-Raphson method to update **e** and return to Step 2.

Step 7: Update the h_{wear} at each node using the Archard wear model.

Step 8: Determine whether the wear evolution has reached the target cycle. If not, return to Step 2 and continue until the target duration is reached.

3. Test scheme

3.1. Scaled test rig for the bottom pivot

A test rig is designed for the scaled bottom pivot specimens, based on the loading conditions and reciprocating rotary motion of the bottom pivot friction pair. As shown in Fig. 7, the rig consists of a control console on the left and a test platform on the right. A hydraulic control system is integrated into the bottom of the console to apply precise loading, including both longitudinal and lateral forces, and is equipped with force sensors to ensure that the applied loads match the designed test conditions. The motor control system is located at the top of the test platform and drives a servo motor to provide rotational motion. The pintle specimen is mounted on the test platform, while the bearing specimen is placed in a dedicated bearing seat, ensuring a stable relative position between the bearing and pintle during testing.

The bearings and pintle used in the tests are 1:10 scale models of the bottom pivot. The bearing has a radius of 60 mm, with a clearance-to-diameter ratio of 1/1000. The bearings are made of high-strength brass, with solid PTFE lubricant embedded on the inner surface and grease injection holes at the top. The bottom pivot pintle is made of forged 34CrNi3Mo steel. It is rigidly connected to the test machine via eight bolts and features a locating hole design to ensure sufficient stability during testing. The structural and material parameters used in the simulation are consistent with those of the experimental test specimens. Table 2 lists the dimensions, loading conditions, and grease parameters of the bottom pivot specimen.

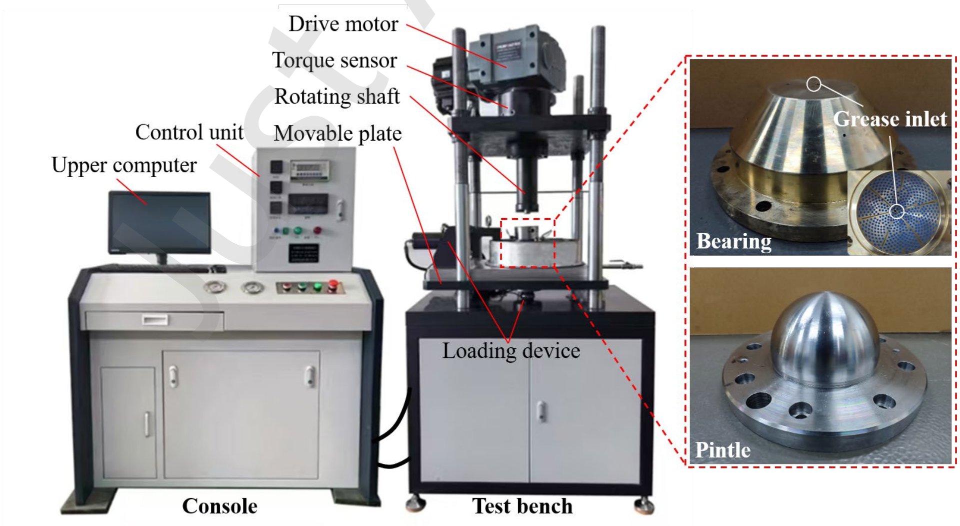

Fig. 7 Schematic diagram of the scaled bottom pivot test rig.

The bottom pivot bearing specimen performs reciprocating rotation on the test rig, maintaining a constant speed 9.135 °/s for most of the time, as shown in Fig. 8 (a).

Each full cycle takes 14.715 s, with acceleration and deceleration phases each lasting 0.015 s. Since these phases are very short relative to the entire cycle, they can be neglected. To monitor the working temperature of the friction pair interface in real time, a temperature sensor is installed 1 mm from the working surface. The temperature results under grease lubrication conditions over the entire 65-hour test are shown in Fig. 8 (b). Considering the long duration of the test, the sensor temperature equilibrates with the interface temperature, so this result can be approximated as the working interface temperature. Due to the low rotational speed of the bottom pivot friction pair, the temperature remains stable throughout the test, ranging from 38.8°C to 42.4°C. Therefore, temperature variations are not separately considered in the simulation, and a constant lubricant viscosity corresponding to 40°C is used as the simulation parameter.

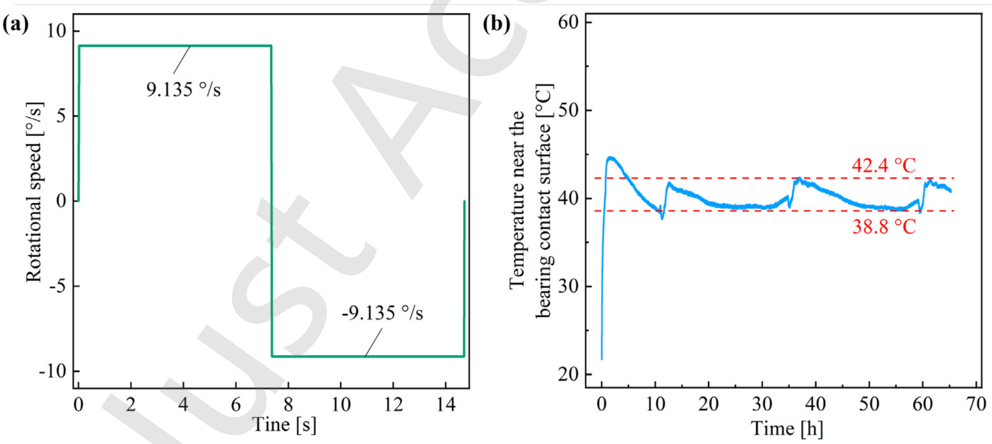

Fig. 8 Conditions during the test: (a) reciprocating rotational velocity; (b) temperature under grease lubrication.

Table 2. Dimensions and test parameters of the bottom pivot test rig.

Parameters	Values	Parameters	Values

Bearing radius (R)	60 mm	Radial clearance (C)	60 μm
Load in x direction (W_x)	39.55 kN	Viscosity of grease (η^*)	0.112 $(Pa \cdot s)^n$
Load in x direction (W_y)	0	Rheological index (n)	0.8
Load in z direction (W_z)	-125.18 kN	Range of rotation	67.5°

3.2. Assembly deformation of the bearing specimen

Based on the actual weight of the miter gate in a hydraulic project, the equivalent vertical and horizontal loads are scaled to 125.18 kN and 39.55 kN, respectively. The vertical load is applied from below by a hydraulic actuator, pushing the pintle specimen upward against the bearing specimen. By the principle of action and reaction, this is equivalent to applying the load from top to bottom. The horizontal load is applied to the bearing specimen from the left side through a loading device. It is worth noting that, to ensure smooth rotation of the bearing during horizontal loading, a deep groove ball bearing is installed on the outside of the bearing seat, which is connected to the horizontal loading device, as shown in Fig. 9 (a).

Under such high loads, assembly deformation d_{as} of the bearing specimen is inevitable, which can affect the bearing clearance and therefore must be considered. An assembly model of the spherical bearing and pintle is established in the finite element software. A fixed constraint is applied to the bottom of the pintle, while vertical and horizontal loads are applied to the top and side of the bearing, as shown in Fig. 9 (b). By extracting the deformation and displacement at the contact interface between the bearing and the pintle, the resulting assembly deformation is obtained and used as an input parameter for the simulation. As shown in Fig. 9 (c), under the combined vertical and horizontal loads, the deformation of the bearing's inner surface ranges from -36.12 μm to 12.966 μm, where negative values indicate inward contraction and positive values indicate outward expansion. In the horizontally loaded region, the deformation is inward due to the larger initial clearance, while the opposite side expands. The top area shows outward expansion because the pintle pushes upward against the bearing.

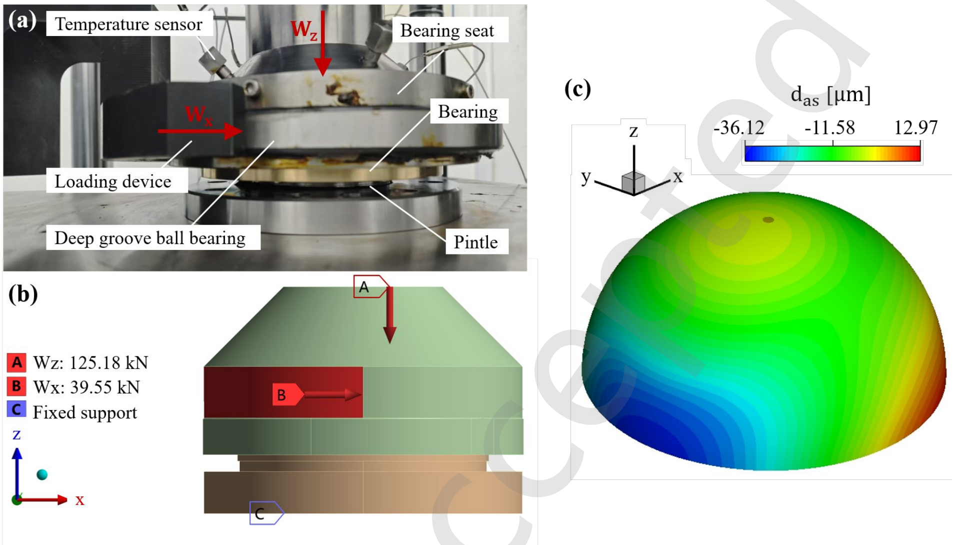

Fig. 9 Loading and assembly deformation of the bearing specimen: (a) test rig loading; (b) simulation loading; (c) assembly deformation.

4. Results and discussion

This section first presents a sensitivity analysis of the model and then investigates the friction and wear characteristics of the bottom pivot bearing under dry friction and grease lubrication conditions, together with the corresponding wear test results.

4.1. Model sensitivity analysis

The non-Newtonian behavior of grease is primarily characterized by the rheological index n. As shown in Fig. 2, rheological test data and curve fitting yield n = 0.8 with a fitting error of ±0.012. To assess the influence of this uncertainty, the grease film pressure p is calculated for n = 0.788, 0.8, and 0.812 under identical operating condition ($e_x = 12$ μm, $e_y = 0$, $e_z = 56$ μm, speed = 9.135 °/s). As shown in Fig. 10 (a), p_{max}=3.45 MPa at n=0.788, p_{max}=3.78 MPa at n = 0.8, and p_{max}=4.11 MPa at n = 0.812. The pressure variation caused by the fitting error is within 9%, indicating that n has a significant influence the pressure. This implies that if a Newtonian model (n = 1) is used to represent the grease, the shear-thinning effect is neglected, resulting in an overestimation of the load-carrying capacity of the grease film.

For the KE statistical contact model, the surface topography parameters ξ, β, and σ are varied by factors of 0.8 and 1.2 relative to their reference values to investigate the influence of parameter variations on contact. The relationship between the dimensionless contact pressure p_c/E and the dimensionless film thickness h/σ is presented in Fig. 10 (b). The results indicate that when h/σ<2 (severe contact regime), the influence of surface topography parameters on contact pressure becomes more pronounced. Therefore, under heavy-load condition, accurate characterization of surface topography is essential for reliable prediction of contact pressure.

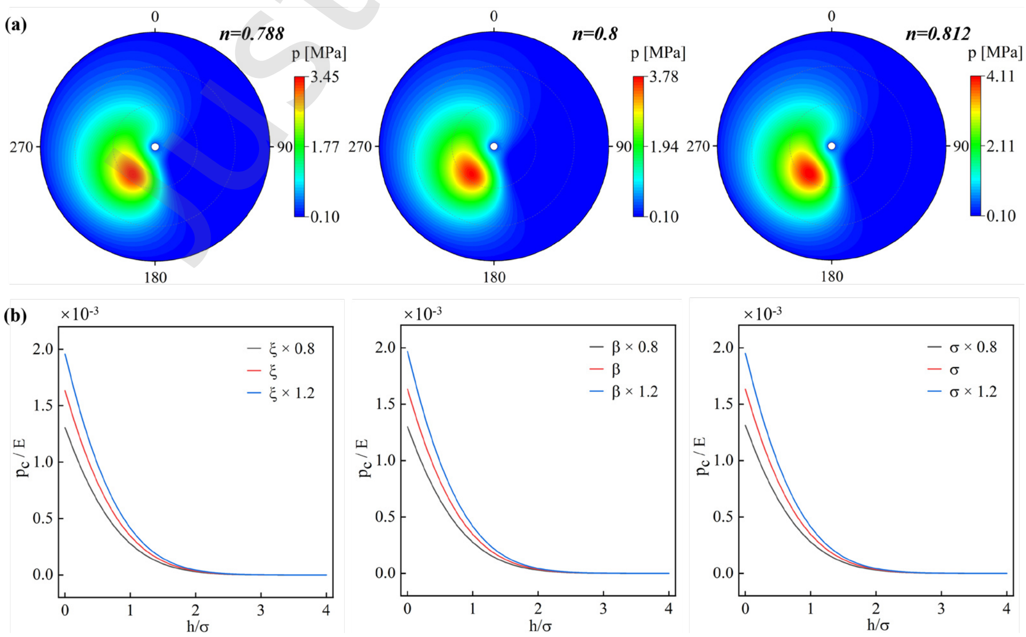

Fig. 10 Sensitivity analysis of grease lubrication and contact models: (a) effect of rheological index

on grease film pressure, (b) effect of surface parameters on contact pressure.

To ensure that the deformation analysis eliminates numerical errors associated with mesh resolution, a mesh independence test is conducted. Four mesh schemes with $\theta \times \varphi$ resolutions of 30×80, 50×100, 70×120, and 100×140 are considered. A uniform pressure of 1 MPa is applied to the spherical bearing, and the resulting deformation is evaluated, as shown in Fig. 11 (a). The results show that when the mesh resolution reaches 70×120, further refinement has a negligible effect on deformation.

Similarly, the mesh independence of the lubrication calculation is verified under the same calculation condition as in Fig. 10, with the results presented in Fig. 11 (b). The relative error in p_{max} between the 70×120 and 100×140 mesh resolutions is only 2%. Therefore, a mesh resolution of 70×120 is adopted to ensure sufficient accuracy while maintaining computational efficiency.

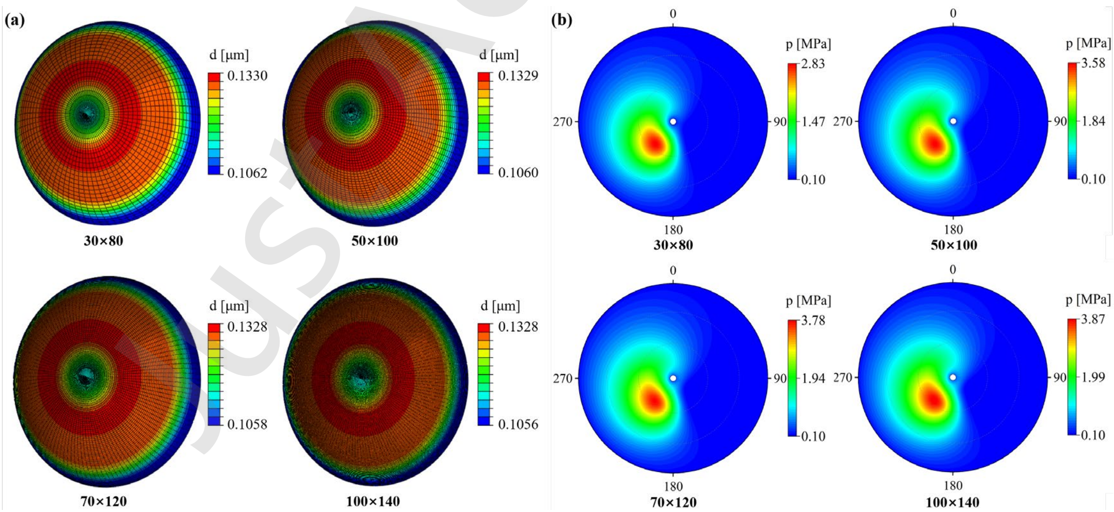

Fig. 11 Mesh independence test: (a) deformation verification; (b) grease film pressure verification.

4.2. Wear evolution under grease-lubricated and dry friction conditions

Fig. 12 shows the simulated wear evolution of the bottom pivot bearing under dry friction after 16000 operating cycles. The wear is mainly concentrated on the top and side surfaces of the bearing, corresponding to the directions of the axial and lateral loads. As the number of cycles increases, the wear depth gradually increases. The maximum wear depths after 3000, 6000, 10000, and 16000 cycles are approximately 8.36 μm, 16.44 μm, 27.09 μm, and 39.71 μm, respectively. In addition, wear under dry friction tends to accumulate along the bearing's side surface. This can be well explained by the Archard wear model, in which wear depth is closely related to the relative sliding distance between the contact surfaces. Since the linear velocity on the side is significantly higher than that on the top, more severe wear occurs on the side surface.

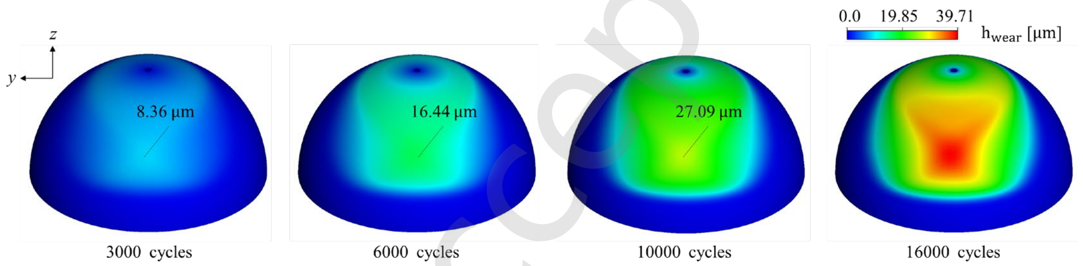

Fig. 12 Wear evolution of the bottom pivot bearing under dry friction (maximum wear reached 39.71 μm after 16000 cycles).

Fig. 13 shows the simulated wear evolution of the bottom pivot bearing under grease lubrication after 16000 operating cycles. Compared to the dry friction case, the wear regions remain similar — mainly concentrated on the top and side surfaces—but the presence of grease significantly reduces the peak wear depth. The maximum wear depths after 3000, 6000, 10000, and 16000 cycles are approximately 5.12 μm, 9.74 μm, 15.99 μm, and 24.03 μm, respectively, showing a 39.5% reduction in peak wear for the grease lubricated bearing compared to the dry friction case. Notably, under grease lubrication, wear also appears on the side surface, but the affected area is narrower than that under dry friction. This is attributed to the higher linear velocity on the side surface, which promotes the formation of a stronger hydrodynamic lubrication film, effectively reducing excessive wear. The mixed EHL results of the bearing will be analyzed in detail in the next section.

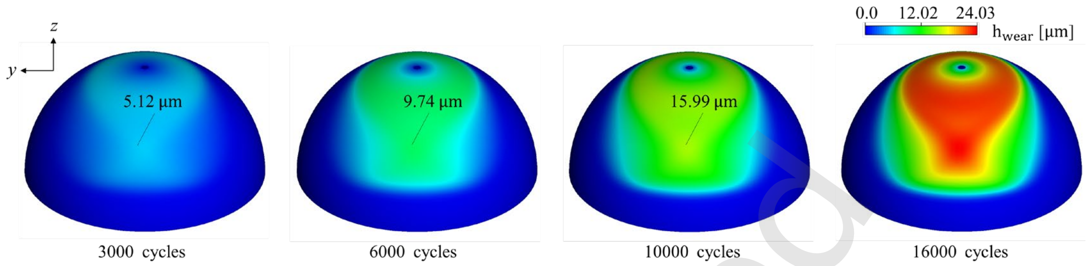

Fig. 13 Wear evolution of the bottom pivot bearing under grease lubrication (maximum wear reached 24.03 μm after 16000 cycles).

4.3. Tribological performance under dry friction and grease lubrication

Fig. 14 illustrates the elastic deformation d_h, clearance (film thickness) h, and contact pressure p_c of an unworn bottom pivot bearing under dry friction. It should be noted that the d_h consists of the assembly deformation d_{as} and the deformation d_c caused by the p_c, as shown in Fig. 14 (a). After achieving force equilibrium in all three directions, the minimum h is 1.27 μm, occurring at the top of the bearing [Fig. 14 (b)]. Due to compression caused by the lateral load, the clearance on the side surfaces is also relatively small. Consequently, the p_c is more pronounced at the top and sides of the bearing [Fig. 14 (c)], with a peak value of 41.8 MPa.

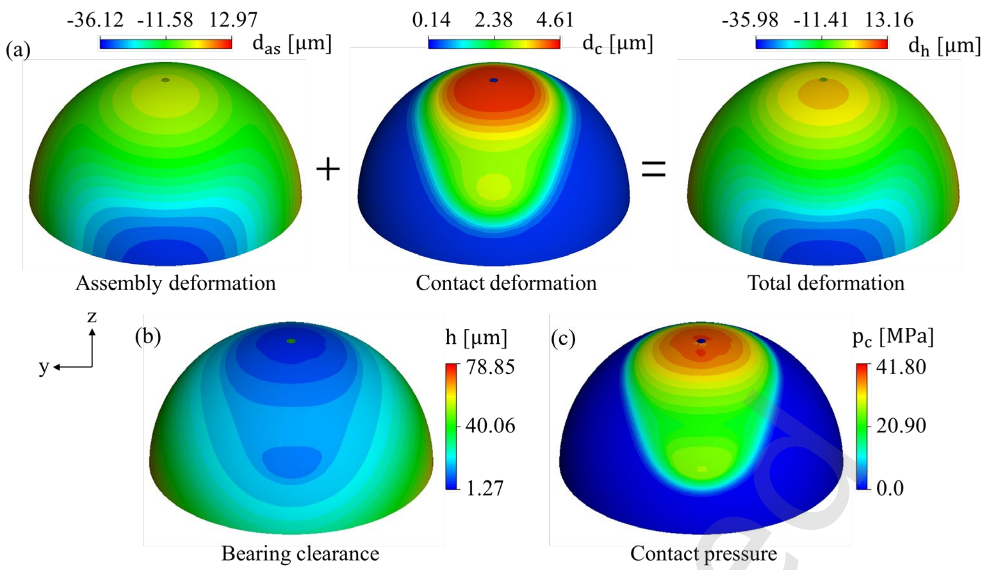

Fig. 14 Tribological fields of the unworn bearing under dry friction: (a) elastic deformation, (b) clearance, and (c) contact pressure.

In the grease lubricated case, the rotation direction affects the pressure distribution due to the inflow direction of the fluid film. As shown in Fig. 15 (a), during forward rotation of the bearing around the z-axis, the grease film pressure concentrates on the left side and reaches up to 13 MPa, generating a deformation (dg) of less than 1 μm. Since d_g is much smaller than d_{as} and d_c, only d_g is shown for clarity. Nevertheless, it increases local film thickness and reduces contact pressure. Fig. 15 (b) shows similar magnitudes for reverse rotation, though with a different distribution. Under grease lubrication, peak contact pressure remains at the top, while lateral pressure is partially replaced by fluid pressure. This is because the surface speed is lowest at the top and increases toward the equator, making hydrodynamic support less effective at the top.

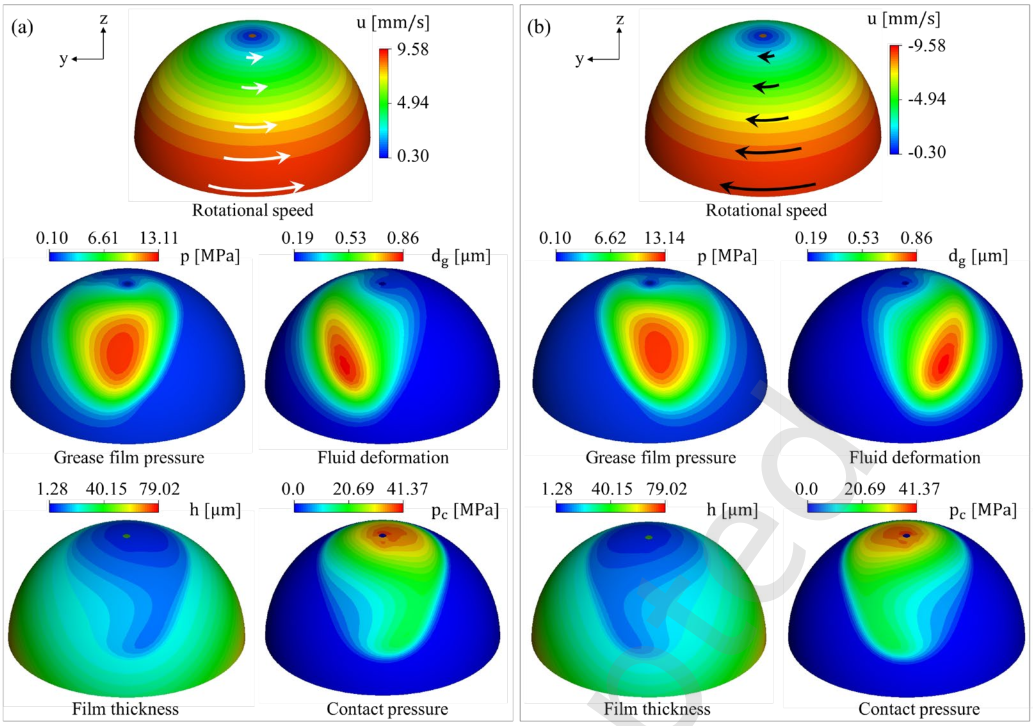

Fig. 15 Tribological fields of the unworn bearing under grease lubrication: (a) forward rotation; (b) reverse rotation.

Furthermore, Fig. 16 shows the evolution of elastic deformation, clearance, and contact pressure of the dry friction bearing after 16000 cycles. A notable phenomenon is that the contact pressure and its induced deformation become more concentrated and intense at the top. This occurs because the sliding distance at the top is relatively short, resulting in less wear, while regions farther from the top experience more severe wear over time, making the top area increasingly prominent. Viewed from the side, part of the loaded region has been worn away, leading to increased clearance and locally reduced contact pressure.

Fig. 17 presents the mixed EHL results of the grease lubricated bottom pivot bearing after 16000 cycles. Figs. 17 (a) and 17 (b) correspond to forward and reverse rotation, respectively. The worn surface profile is clearly reflected in the fluid pressure distribution, which becomes irregular. The elastic deformation d_g caused by the grease film pressure p also becomes more elongated. Both the film thickness h and contact pressure p_c exhibit significant asymmetry. Similar to the dry friction case, the p_c at the top becomes higher and more concentrated. However, under grease lubrication, the peak p_c is about 73 MPa, which is 14% lower than the 85 MPa observed under dry friction. This reduction is mainly due to the milder wear under the support of the fluid film, resulting in a less pronounced protrusion at the top region.

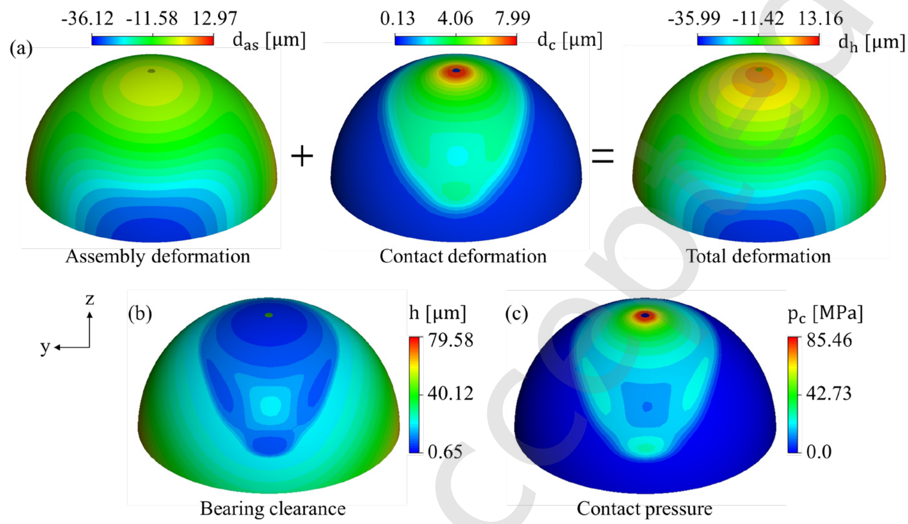

Fig. 16 Tribological fields of the worn bearing under dry friction: (a) elastic deformation, (b) clearance, and (c) contact pressure.

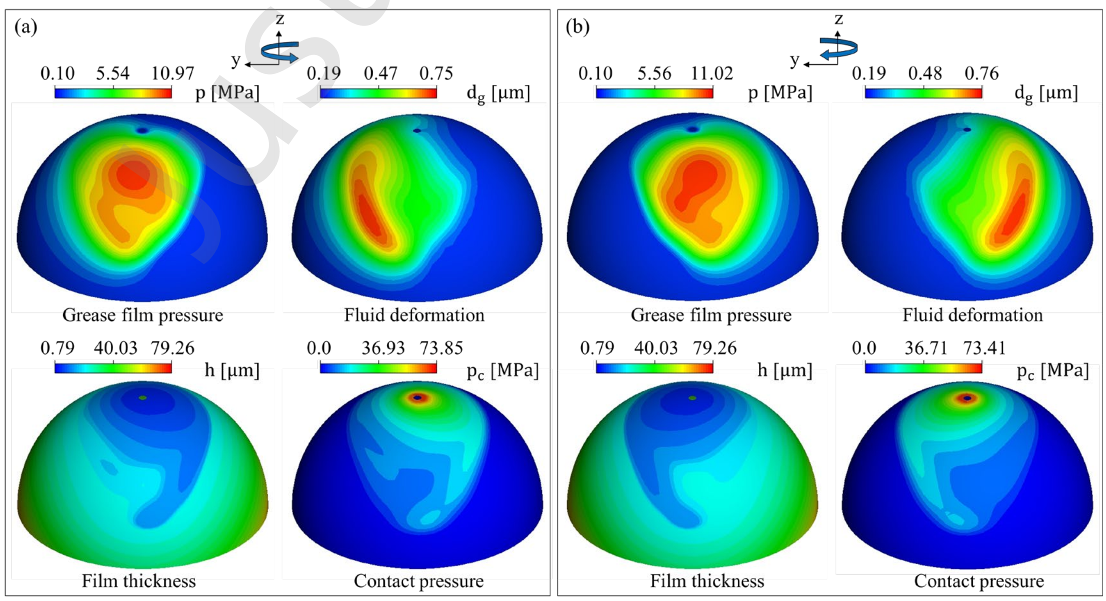

Fig. 17 Tribological fields of the worn bearing under grease lubrication: (a) forward rotation; (b)

reverse rotation.

Fig. 18 shows the contact force F_c and grease film force F_g of the bottom pivot bearing over 16000 cycles under dry and grease lubricated conditions. Fig. 18 (a) presents the forces in the x-direction. Under dry friction, only contact force exists, F_{cx} maintaining around -39.55 kN to achieve load balance. Under grease lubrication, the F_{cx} is about -22.5 kN and the F_{gx} is -17.1 kN, with the latter contributing nearly 43% of the load support. Fig. 18 (b) shows the forces in the z-direction. Under dry friction, the F_{cz} reaches 125.18 kN, while under grease lubrication, the F_{cz} and F_{gz} are approximately 98 kN and 27 kN, respectively, with the latter bearing about 22% of the load. These results confirm that load equilibrium is maintained during the wear evolution analysis of the bottom pivot bearing, and that the grease film force plays a more significant role in the x-direction.

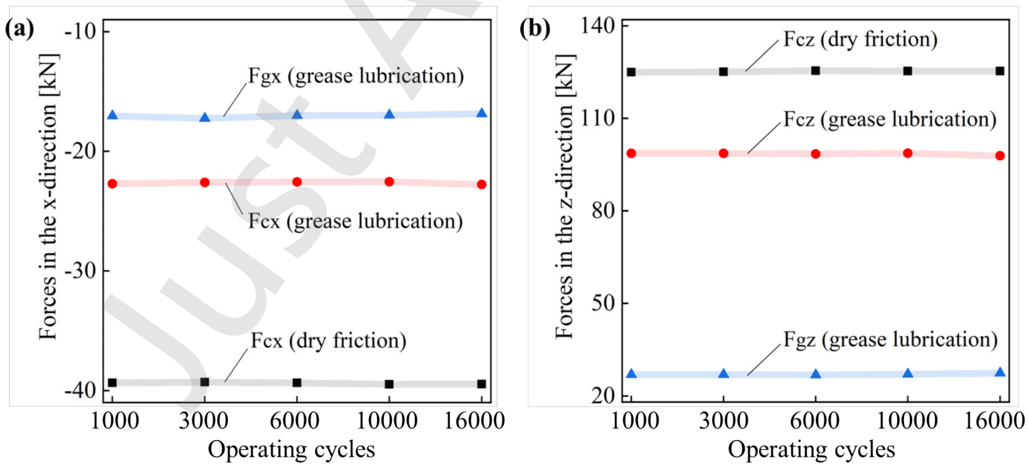

Fig. 18 Contact force and grease film force during the operation of the bottom pivot bearing: (a) x-direction; (b) z-direction.

4.4. Experimental Validation

A long-cycle wear test is conducted on a scaled bottom pivot bearing samples using the test rig. After 16000 reciprocating cycles, wear on the bearing is observed. Fig. 19 shows the results under dry friction and grease lubrication. Under dry friction conditions, part of the embedded self-lubricating material is worn out, forming a distinct transfer film. In contrast, under grease lubrication, the transfer film in the worn regions is uneven and the surface appears moist, indicating that grease is incorporated into the film. In both cases, wear appears in the dome region of the bearing, but the polar point shows less wear, confirming the contact pressure distributions shown in Figs. 16 and 17. Moreover, under dry friction, the bearing exhibits a larger wear area, mainly on the side surface, whereas the grease lubricated bearing shows relatively smaller wear on the side. A comparison between the simulated wear (top views in Figs. 12 and 13) and experimental wear confirms good consistency: (1) the overall wear patterns match, reflecting both vertical and lateral loading; (2) the side wear under dry friction is more severe than under grease lubrication. This confirms the reliability of the simulation model.

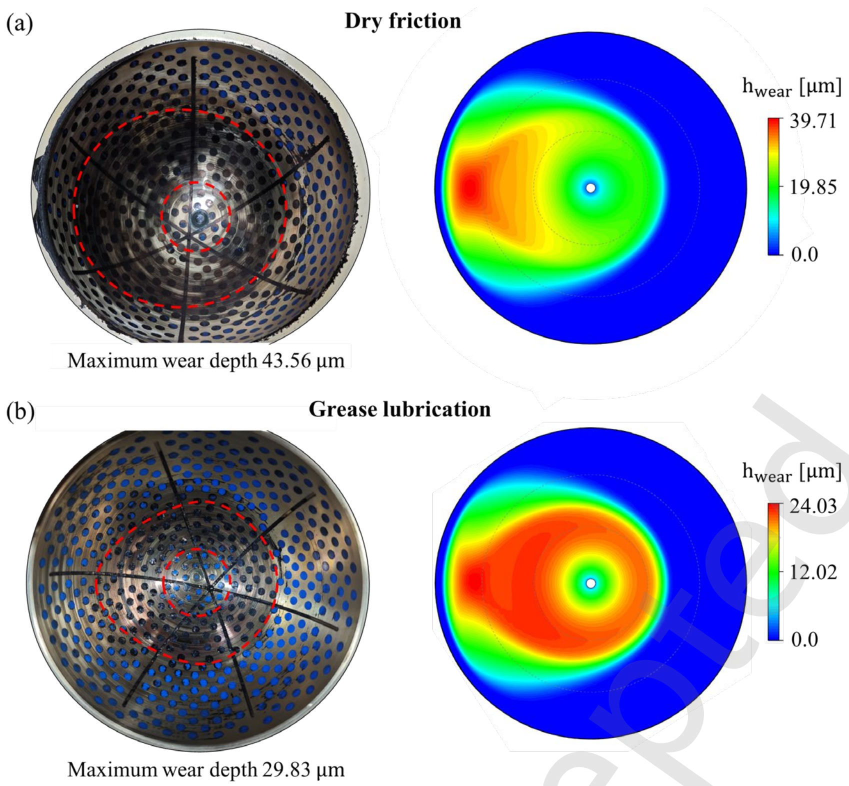

Fig. 19 Experimental and simulated wear distribution maps: (a) dry friction; (b) grease lubrication.

The worn regions of the spherical bearing appear black, corresponding to transfer films generated by the worn PTFE solid lubricant. As shown in Fig. 19, under dry friction conditions the transfer film spreads extensively over the bearing surface, whereas under grease lubrication its formation is significantly restricted. Fig. 20 further presents the morphology of the pintle after the long-term tests, where Figs. 20 (a) and (b) show the side and top views under dry friction, and Figs. 20 (c) and (d) depict the corresponding morphology under grease lubrication.

As illustrated in Figs. 20 (a) and 20 (c), part of the PTFE debris settles at the bottom of the pintle due to gravity. Under grease lubrication, however, the debris mixes with the grease and fails to develop into an effective solid lubricating film, leading to considerable deposits at the specimen bottom. This suggests that grease can hinder the formation of PTFE transfer films. Furthermore, once the grease is depleted or its properties deteriorate during long-term service (well beyond 16000 cycles), the performance of the friction-pair may decline sharply, partly because grease lubrication suppresses the establishment of solid transfer films.

Figs. 20 (b) and 20 (d) also indicate that the conditions at the pintle apex are similar under both lubrication states. Owing to the extremely low rotational linear velocity at the top, the apex is insufficiently run-in with the bearing, which explains the concentration of contact pressure observed in Figs. 16 and 17. It can therefore be inferred that with prolonged reciprocating tests, the unrun-in apex would become more pronounced and could eventually detach as a result of fretting wear or crushing. Nevertheless, the present test duration has not yet reached this stage.

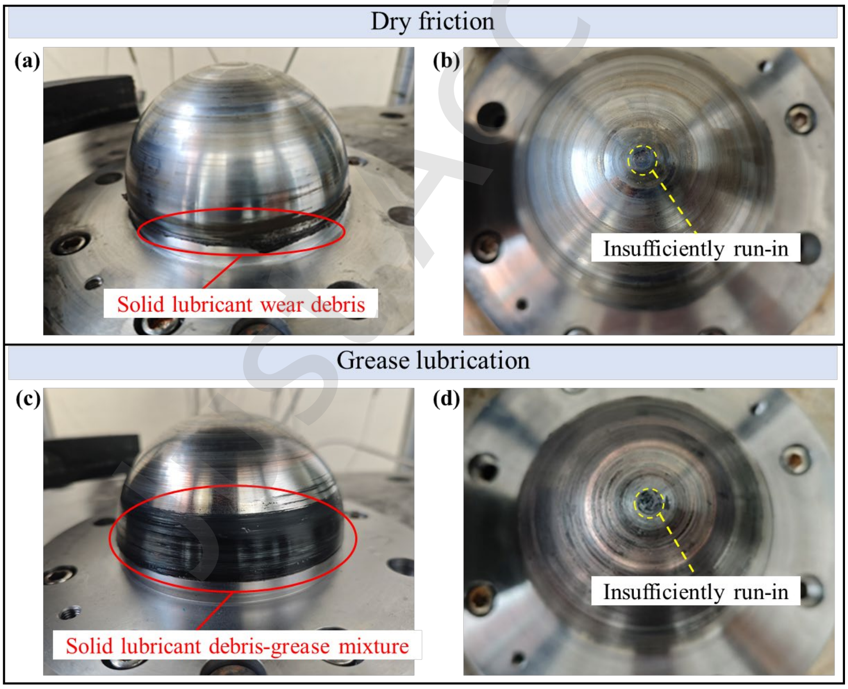

Fig. 20 Views of the pintle after the test: (a) and (b) under dry friction; (c) and (d) under grease lubrication.

The wear depth of typical regions on the bottom pivot bearing specimens is measured using a coordinate measuring machine (VGS V3-696) with an accuracy of 2 μm. Fig. 21 (a) shows the measurement setup, and Fig. 21 (b) presents the distribution of 189 measured points. The experimental average wear depth is obtained by calculating the mean of these points, and the simulated wear depth is averaged in the same manner. Fig. 21 (c) compares the experimental and simulated results under the two lubrication conditions: under dry friction, the experimental and simulated values are 32.03 μm and 28.06 μm, respectively; under grease lubrication, the corresponding values are 21.93 μm and 20.81 μm. The close agreement indicates that the model effectively captures the wear behavior under different lubrication states. The experimental results show that grease lubrication reduces the average wear depth by 31.5%, while the simulation predicts a reduction of 25.8%. This consistency not only confirms the anti-wear effect of grease under the tested conditions but also validates the reliability and predictive accuracy of the developed model.

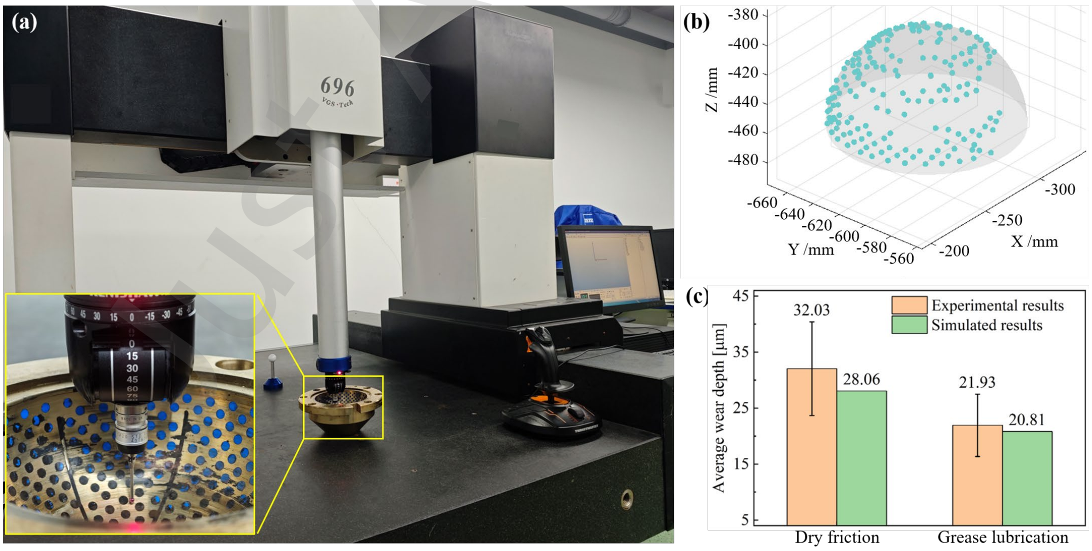

Fig. 21 Characterization of wear depth on the bottom pivot bearing specimen: (a) coordinate measuring machine; (b) captured measurement points; (c) comparison between simulation and experimental results.

Overall, the simulation framework proposed in this study provides an effective tool for evaluating wear performance and estimating the service life of bottom pivot bearings under lubricated conditions. It also offers valuable guidance for the optimization of lubrication strategies and structural design, contributing to improved durability, reduced maintenance frequency, and enhanced reliability of miter gate systems in practical engineering applications.

5. Conclusions

To investigate the effect of grease lubrication on the wear performance of the bottom pivot friction pair in miter gates, this study develops a theoretical and experimental framework. The main conclusions are as follows:

(1) A Reynolds equation for non-Newtonian grease is derived in spherical coordinates, addressing the lack of lubrication models for non-Newtonian fluids in spherical geometries. A coupled analysis method for mixed elastohydrodynamic lubrication and wear is further developed, accounting for large deformations under heavy loads and enabling more physically consistent predictions of lubrication and wear evolution on spherical pivot bearings. The proposed method is validated through long-term experiments on scaled specimens.

(2) The model reveals that grease provides region-selective protection to the bearing, with significantly greater effectiveness on the side surface than at the apex, due to the higher sliding velocity that promotes hydrodynamic pressure generation. This leads to a more uniform wear distribution and a 39.5% reduction in maximum wear depth after 16000 cycles compared with dry friction, showing good agreement with

experimental measurements.

(3) A practical trade-off is identified: grease effectively reduces early-stage wear, but its long-term degradation and interference with solid-lubricant transfer films can compromise bearing performance, making periodic replenishment necessary. The model applies to low-speed, heavy-load spherical bearings with minimal temperature variations (e.g., miter gate bottom pivots, hydraulic spherical plain bearings), but its accuracy is limited under high-speed or significant temperature-variation conditions where viscosity-temperature and inertial effects become non-negligible.

Funding:

This study is supported by the National Natural Science Foundation of China (Grant No. 52405209, 52130502).

Conflict of Interest:

The authors declare no conflict of interest.

References

[1] Daniel R A. Recent structural developments in miter gates for navigation locks. *Maritime Engineering and Soil Technology* **6**: 304-315 (2017). https://imig.pl/pliki/artykuly/2017-6/2017-6_304-315_Daniel.pdf.

[2] Fillmore T B, Wang S, Thurmer C, Eick B A, Spencer B F. Multi-modal model updating of miter gates on navigational locks, *Struct Health Monit* **24**: 2209-2228 (2025).

[3] Zeng Y, Zhao Z, Qian G, Todd M D, Hu Z. Enhancing bayesian inference-based damage diagnostics through domain translation with application to miter gates, *J Mech Design* **147**:

061701 (2025).

[4] Wang J, An X. Research on prediction method of metal structure camber of miter gate in ship lock. *Advances in Machinery, Materials Science and Engineering Application X* **58**: 937-942 (2024). https://ebooks.iospress.nl/doi/10.3233/ATDE240727.

[5] Wang S, Fillmore T, Lee J, Eick B A, Spencer B F. Reference-free ego-motion compensation for vision-based measurement of structural deformations of miter gates. *Struct Health Monit* **24**: 2193-2208 (2025).

[6] Chen Z, Rose A, Roberts F, Tucci A. Regional supply-chain impacts of Mississippi River fertilizer shipments disrupted by climate change. *Risk Anal* **45**: 3090-3109 (2025). https://doi.org/10.1111/risa.70064.

[7] Li J, Hu Y, Wang X, Diao M. Operation safety evaluation system of ship lock based on extension evaluation and combination weighting method. *J Hydroinform* **25**: 755-781 (2023).

[8] Xiang X, Yun Z, Biao L, Ze F, Wang X, Zhao X, et al. Analysis and evaluation of the spreading mechanism of solid lubricant under low-speed and heavy-load graphite inlay lubrication. *Tribology* **44**: 1283-1294 (2024).

[9] Xiang X, Zu Z, Wang X, Bai H, Qin H, Zhao X. Experimental study on friction characteristics of miter gate bottom pivot with different solid lubrication. *Tribology* **42**: 1044-1052 (2021).

[10] Ming Y, Zhao Z, Jun Y, Wei J, Pei L, Liu W. Research status and prospect of self-lubricating fabric composites and their applications in self-lubricating spherical plain bearings. *Tribology* **44**: 396-420 (2024).

[11] Paulus T, Medina V, Keyser T, Rundgren B, Hess M, Sills J. Mechanical equipment lubrication standardization and sustainability inland navigation design center, *Rock Island INDC TR-2018-*

1 2018-03. (2018).

[12] Qin H, Guo W, Li X, Zhao X, Xu X. Tribological performance of gate bottom pivot friction pair QT600-3/40Cr and its wear surface power spectral density characterization. *J Mech Eng* **55**: 102-109 (2019).

[13] Xu X, Feng Z, Xiao N, Zhao X, Zhang Z. Planar reconstruction of regular surfaces' three-dimensional morphology and tribology application. *Lubricants* **11**: 398 (2023).

[14] Jhurani S M, Higgs III C F. An elastohydrodynamic lubrication (EHL) model of wear particle migration in an artificial hip joint. *Tribol Int* **43**: 1326-1338 (2010).

[15] Wu Z, Gao L, Huang X, Hua Z. Simulation study on the surface texturing design of coc hip joints based on elastohydrodynamic lubrication model. *Lubricants* **13**: 217 (2025).

[16] Xu X, Guan Z, Li Z, Sulowicz M, Królczyk G, Dai T, et al. Machine learning calculation model for hydrodynamic lubrication characteristics of a miter gate bottom pivot. *Eng Anal Bound Elem* **142**: 1-9 (2022).

[17] Li J, An L, Huang Y, Li Z, Guan B, Li R. Effect of operating conditions and surface roughness on grease lubrication efficiency. *Therm Sci Eng Prog* **50**: 102577 (2024).

[18] Wang Y, Xu Y, Sheng X, Xie G, Zhang Y. Analysis of lubrication and wear model with grease for the harmonic reducer. *ASME J Tribol* **147**: 091118 (2025).

[19] Cheng S, Zhang R, Meng X, Zheng L, Liu Z. Tribological analysis of rotor system startup considering deformations of high elastic rubber bushings and grease lubricated plastic bearings. *Proc Inst Mech Eng Part J J Eng Tribol* **239**: 451-466 (2025).

[20] Zhao X, Su D, Xu X, Dong Y, Gong Z. Study on surface wear of gate bottom pivot based on multi-notch measurement. *Wear* **462**: 203519 (2020).

[21] Zhao M, Wang J, Qin X, Kang X, Wang R. Study on the miter gate fault diagnosis methods based on vibration signals. *Adv Mater Res* **875**: 2087-2091 (2014).

[22] Qin H, Guo W, Xu X, Yuan Z, Zhao X. Evaluation of wear and failure of gate bottom pivot friction pairs under grease lubrication. *China Mech Eng* **30**: 650 (2019).

[23] Oh K, Huebner K. Solution of the elastohydrodynamic finite journal bearing problem. *J Lubr Technol* **95**: 342-351 (1973).

[24] Bouyer J, Fillon M. On the significance of thermal and deformation effects on a plain journal bearing subjected to severe operating conditions. *ASME J Tribol* **126**: 819-822 (2004).

[25] Cheng S, Meng X, Yin J, Yang L, Zhang J. Configuration performance of main shaft bearings for transient-loaded wind turbine. *Int J Mech Sci* **293**: 110171 (2025).

[26] Chen S, Guo F, Wang W, Wang Y. An improved mixed lubrication model for revealing the mechanism of high speed and frictional heat on sealing performance. *Tribol Int* **191**: 109147 (2024).

[27] Zhang X, Wang Y, Wang K, Jin H, Liu W, Li Z. Nonlinear vibration of a propeller propulsion shafting with frictional and magnetic excitations of journal and thrust bearings. *Mech Syst Sig Process* **230**: 112660 (2025).

[28] Wang D, Li D, He X, Dong J, Zang G, Guo Y, et al. Theoretical analyses and experimental research on micro-nano composite magnetorheological grease for sealing liquids with different viscosities. *Tribol Int* **201**: 110265 (2025).

[29] Zhang X, Jiang N, Zhou Y, Han B, Zhu Y, Yan K, et al. Numerical simulation method of grease flow in a grease groove with experimental validation. *Tribol T* **68**: 142-155 (2025).

[30] Wang D, Yang J, Wei P, Pu W. A mixed EHL model of grease lubrication considering surface

roughness and the study of friction behavior. *Tribol Int* **154**: 106710 (2021).

[31] Mubashshir M, Shaukat A. The role of grease composition and rheology in elastohydrodynamic lubrication. *Tribol Lett* **67**: 104 (2019).

[32] Gong J, Yan H, Meng F, Jing X. Thermal-elastohydrodynamic lubrication study of axial-modified greased cycloid drive in rotate vector reducer. *Tribol Int* **185**: 108488 (2023).

[33] Wu M, Han X, Tao Y, Pei J. A mixed EHL analysis method for grease and formulas for film thickness and asperity load. *Tribol Lett* **70**: 128 (2022).

[34] Goenka P, Booker J. Spherical bearings: static and dynamic analysis via the finite element method. *J Lubr Technol* **102**: 308-318 (1980).

[35] Askari E, Andersen M. A modification on velocity terms of Reynolds equation in a spherical coordinate system. *Tribol Int* **131**: 15-23 (2019).

[36] Patir N, Cheng H. An average flow model for determining effects of three-dimensional roughness on partial hydrodynamic lubrication. *J Lubr Technol* **100**: 12-17 (1978).

[37] Patir N, Cheng H. Application of average flow model to lubrication between rough sliding surfaces. *J Lubr Technol* **101**: 220-229 (1979).

[38] Kogut L, Etsion I. Elastic-plastic contact analysis of a sphere and a rigid flat. *J Appl Mech* **69**: 657-662 (2002).

[39] Cheng S, Meng X, Li R, Liu R, Zhang R, Sun K, et al. Rough surface damping contact model and its space mechanism application. *Int J Mech Sci* **214**: 106899 (2022).

[40] Archard J F. Contact and rubbing of flat surfaces. *J Appl Physics* **24**: 981-988 (1953).

[41] Blanco J, Porteiro J, López J, Cortada M, Fernández S. Wear protection assessment of ultralow viscosity lubricants in high-power-density engines: A novel wear prediction algorithm. *Friction*

12: 1785-1800 (2024).

[42] Harnafi M, Guidault P, Boucard P, Paleczny C. A simplified model for the wear prediction of plain bearings in the variable stator vane system. *Tribol Int* **196**: 109667 (2024).

[43] Wang Z, Pu W, Pei X, Cao W. Contact stiffness and damping of spiral bevel gears under transient mixed lubrication conditions. *Friction* **10**: 545-559 (2022).